SIAM J. SCI. COMPUT.
Vol. 46, No. 6, pp. B785–B805

MCMS-RBM: MULTICOMPONENT MULTISTATE REDUCED BASIS METHOD TOWARD RAPID GENERATION OF PHASE DIAGRAMS FOR THE LIFSHITZ–PETRICH MODEL*

YAJIE JI†, LIJIE JI‡, YANLAI CHEN§, AND ZHENLI XU¶

Abstract. Due to quasicrystals having long-range orientational order but without translational symmetry, traditional numerical methods usually suffer when applied as is. In the past decade, the projection method has emerged as a prominent solver for quasiperiodic problems. Transforming them into higher-dimensional but periodic ones, the projection method facilitates the application of the fast Fourier transform. However, the computational complexity inevitably becomes high, which significantly impedes, e.g., the generation of the phase diagram since a high-fidelity simulation of a problem whose dimension is doubled must be performed for numerous times. To address the computational challenge of quasiperiodic problems based on the projection method, this paper proposes a multicomponent multistate reduced basis method (MCMS-RBM). Featuring multiple components with each providing reduction functionality for one branch of the problem induced by one part of the parameter domain, the MCMS-RBM does not resort to the parameter domain configurations (e.g., phase diagrams) a priori. It enriches each component in a greedy fashion via a phase transition guided exploration of the multiple states inherent to the problem. Adopting the empirical interpolation method, the resulting online-efficient method vastly accelerates the generation of a delicate phase diagram to a matter of minutes for a parametrized two-turn-four dimensional Lifshitz–Petrich model with two length scales. Moreover, it furnishes surrogate and equally accurate field variables anywhere in the parameter domain.

Key words. reduced basis method, projection method, quasicrystals, fast Fourier transform, empirical interpolation method, phase diagram

MSC codes. 65M70, 35Q99, 65T50

DOI. 10.1137/23M1596831

1. Introduction.

In the 1980s, Shechtman et al. [32] observed a metallic phase with long-range orientational order in a rapidly cooling Al-Mn alloy. Unlike the periodic structures that feature translational symmetries or 1-, 2-, 3-, 4-, and 6-fold rotational symmetries, this new structure has a 5-fold rotational symmetries. Later, researchers coined this new long-range ordered structure "quasicrystals" [23]. Since the discovery of the 5-fold quasicrystals, more different structures with 5-, 6-, 8-, 12-, and 20-fold symmetries have emerged in various metallic alloys [33, 36]. There have

*Submitted to the journal's Software, High-Performance Computing, and Computational Science and Engineering section August 28, 2023; accepted for publication (in revised form) July 16, 2024; published electronically November 4, 2024.

https://doi.org/10.1137/23M1596831

Funding: The second author acknowledges the support from NSFC grant 12201403 and China Postdoctoral Science Foundation 2021M702141. The third author is partially supported by National Science Foundation grant DMS-2208277 and by the UMass Dartmouth MUST program, N00014-20-1-2849, established by Dr. Ramprasad Balasubramanian via sponsorship from the Office of Naval Research. The fourth author acknowledges support from the NSFC (grant 12071288). The authors also acknowledge the support from the HPC center of Shanghai Jiao Tong University.

†School of Mathematical Sciences, Shanghai Jiao Tong University, Shanghai 200240, China (jiyajie595@sjtu.edu.cn).

‡Corresponding author. School of Mathematical Sciences, Shanghai Jiao Tong University, Shanghai 200240, China (sjtujidreamer@sjtu.edu.cn).

§Department of Mathematics, University of Massachusetts Dartmouth, North Dartmouth, MA 02747 USA (yanlai.chen@umassd.edu).

¶School of Mathematical Sciences, CMA-Shanghai, and MOE-LSC, Shanghai Jiao Tong University, Shanghai 200240, China (xuzl@sjtu.edu.cn).

also been certain soft quasicrystals in soft matter systems [15, 27, 28, 35, 40, 41]. Since their discoveries, these quasicrystals have been widely used in materials science, thermal engineering, metallurgical engineering, photonics, and energy storage [36, 40, 41].

In order to understand the formation, stability, and various physical properties of different quasicrystals, some theoretical and numerical methods have been proposed. For the theoretical model, Lifshitz and Petrich first proposed the Lifshitz–Petrich (LP) model to explain the 12-fold symmetry excited by dual-frequency filtering in the Faraday experiment [25]. Subsequently, the LP model has been used to study the stability of the two-dimensional 5-, 8-, and 10-fold quasicrystals with two characteristic wavelength scales [20]. The LP model represents a coarse-grained mean field theory. It assumes that the free energy of the system can be represented as a function of the order parameters. There are two such parameters, with one representing the temperature and the other delineating the asymmetry of the order parameter. When these two parameters vary, the quasicrystals exhibit a rich phase behavior containing a number of equilibrium ordered phases. This phase diagram, when captured well, can be used to study the transition path between different structures. For example, the LP model describing the 12-fold quasicrystals in two dimensions also includes the 6-fold crystalline state (C6), the lamellar quasicrystalline state (LQ), the transformed 6-fold crystalline state (T6), and the Lamella state (Lam) [39]. The structures of these stable states are shown in real and the so-called reciprocal spaces, respectively, in Figure 1.

It is therefore imperative to simulate these quasicrystals accurately across the entire parameter domain. That proves extremely challenging for two reasons. First, each simulation is delicate and costly. Unlike periodic structures that are translation invariant and therefore can be calculated in a unit cell with periodic boundary conditions, quasicrystals are rotationally invariant but not translationally invariant. This makes it difficult to determine the computational domain and boundary conditions. Second, the need for repeated simulations exacerbates the situation. To resolve the phase diagram even on a relatively small parameter domain, thousands of simulations are needed.

There are two popular methods to overcome the first challenge: the crystaline approximation method (CAM) [25, 42] and the projection method (PM) [21]. The CAM approximates the quasicrystals with a periodic structure, and the size of the computational domain increases rapidly as the accuracy of approximation becomes higher. This has been systematically illustrated in several papers, and readers can refer

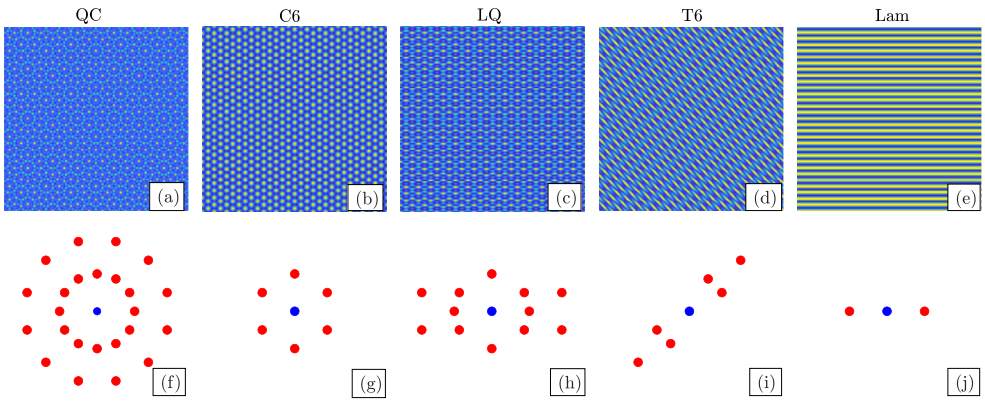

FIG. 1. *Order parameters (top) and the corresponding prominent diffraction patterns in the reciprocal space (bottom) for QC (af), C6(bg), LQ(ch), T6(di), and Lam(ej) states.*

to [21]. The PM utilizes the fact that the reciprocal vectors of a quasicrystal in a lower-dimensional space can be approximated by a linear combination of basic reciprocal vectors in a higher-dimensional space. This technique renders the quasicrystal periodic in a higher-dimensional space [38]. With this idea, the Fourier expansion approach can be employed for the quasiperiodic systems [11, 20, 21, 22, 43]. This projection method is performed in a high-dimensional space and can use the fast Fourier transform. For the two-dimensional LP model with two length scales, the phase diagram is quite complicated due to the wide range of parameter values and large number of possible stable states. It is severely time consuming if one wants to generate the phase diagram for a wide range of parameters accurately [30]. This is an especially onerous task if the physical and/or parametric domain are of high dimensions. Although an adaptive method exists [18] that can generate the phase diagram without having to resolve the full parameter domain, it fails to produce the field variables which are needed, e.g., in controlling the self-assembly of quasicrystals and a variety of other desired structures in practical experimental realizations [1, 5, 24, 29]. Moreover, if there are five possible stable states for each unknown parameter, one needs to solve the LP model five times with respect to five different initial values and then choose the one having the minimum free energy as the stable state. Therefore, the pursuit of efficient numerical algorithms for the parametric LP model has emerged as a prominent research focus.

To achieve that goal while dealing with the second challenge, we propose in this paper a multicomponent multistate reduced basis method (MCMS-RBM) as a generic framework for reduced order modeling for parametric problems whose solution has multiple states across the parameter domain. The RBM [16, 30, 31] is a projection-based model order reduction technique that provides a mathematically accurate surrogate solution in a highly efficient manner and is capable of reducing the computational complexity of the full order model (FOM) by several orders of magnitude after an offline learning stage. It was first introduced for a nonlinear structure problem in the 1970s [26] and has been later analyzed and extended to solve many problems, such as the linear evolutionary equation [14], viscous Burgers' equation [37], and Navier–Stokes equations [10], among others. Its extension to the reduced over collocation setting [6, 7, 8] makes available a robust and efficient implementation for the nonlinear and nonaffine setting. The offline-online decomposition, often assisted by the empirical interpolation method (EIM) [2, 12], is a critical approach to realize online efficiency, meaning the online solver is independent of the degrees of freedom of the FOM. We adopt PM, as opposed to CAM, for our underlying FOM due to its superiority of approximating quasiperiodic structures by periodic ones, albeit in a higher dimension. For consistency among the states, we solve the higher-dimensional problems even when the structure is periodic (e.g., for C6, T6, and Lam). The proposed MCMS-RBM has two prominent features in comparison to the standard RBM. First, it has multiple components with each providing reduction functionality for one branch of problem induced by one part of the parameter domain. Thanks to this feature, the method has the potential of solving other parameterized problems whose solution manifold features multiple braches, such as bifurcation problems. Second, without resorting to the parameter domain configurations (e.g., phase diagrams) a priori, it enriches each component in a greedy fashion. With the existence of multiple stable states and the occurrences of phase transitions, it is difficult to construct precise low dimesnional RB spaces for each candidate state. The MCMS-RBM overcomes this difficulty by leveraging the structures of the prominent reciprocal vectors of all possible stable states and designing a phase transition indicator. This indicator guides the greedy algorithm to explore the multiple states inherent to the quasicrytal problem.

The rest of this paper is organized as follows. In section 2, we introduce the parametrized LP model, the projection method, the pseudospectral method used to obtain the high-fidelity solution, the phase diagram, and the criteria of phase transition. The key components of the MCMS-RBM, including the online and offline procedures and the EIM process, are introduced in section 3. We then present numerical results in section 4 to demonstrate the efficiency and accuracy of the proposed MCMS-RBM. Finally, concluding remarks are drawn in section 5.

2. Lifshitz–Petrich model and the projection method. In this section, we introduce the Lifshitz–Petrich model with two characteristic length scales and the phase-steady full order solutions based on the projection method.

2.1. Lifshitz–Petrich model. The LP model is based on the Swift–Hohenberg model [34] and the Landau–Brazovskii model [3], which are widely used in the study of materials science and polymeric systems, respectively. The LP model extends one wavelength scale of the Swift–Hohenberg equation to two characteristic wavelength scales. The scalar order parameter $\phi(\boldsymbol{r})$ describes how perfectly the molecules are aligned. It minimizes the corresponding free energy functional, which is defined as

$$\mathcal{F}(\phi; c, q, \boldsymbol{\mu}) = \int_V dr \left\{ \frac{c}{2} |\left(\nabla^2 + 1^2\right)\left(\nabla^2 + q^2\right)\phi|^2 - \frac{\varepsilon}{2}\phi^2 - \frac{\alpha}{3}\phi^3 + \frac{1}{4}\phi^4 \right\}, \tag{2.1}$$

where $\boldsymbol{r} \in \mathcal{R}^d$ with $d = 2$, V is the system volume, c is an energy penalty parameter to ensure that the principle reciprocal vectors of structures is located on $|\boldsymbol{k}| = 1$ and $|\boldsymbol{k}| = q$, with q being an irrational number depending on the symmetry, ε is the reduced temperature, and α is a phenomenological parameter. For simplicity, we define $\boldsymbol{\mu} := [\varepsilon, \alpha]$, a two-dimensional parameter vector, and denote the last two nonlinear terms of (2.1) and their negative derivative as

$$h(\phi; \boldsymbol{\mu}) = -\frac{\alpha}{3}\phi^3 + \frac{1}{4}\phi^4, \quad g(\phi; \boldsymbol{\mu}) = \alpha\phi^2 - \phi^3.$$

For a given parameter $\boldsymbol{\mu}$, the candidate stable states are the local minima of the free energy functional, that is, the solutions of the Euler–Language equation

$$\frac{\delta \mathcal{F}}{\delta \phi} = 0. \tag{2.2}$$

This is an eighth-order nonlinear partial differential equation. To solve it, one can use the gradient flow method [19, 20]

$$\frac{\partial \phi}{\partial t} = -\frac{\delta \mathcal{F}}{\delta \phi} = -\left[c\left(\nabla^2 + 1\right)^2 \left(\nabla^2 + q^2\right)^2 \phi - \varepsilon\phi \right] + g(\phi; \boldsymbol{\mu}), \tag{2.3}$$

which is then discretized by the following implicit-explicit scheme:

$$\frac{\phi^{n+1} - \phi^n}{\Delta t} = -\left[c\left(\nabla^2 + 1\right)^2 \left(\nabla^2 + q^2\right)^2 \phi^{n+1} - \varepsilon\phi^n \right] + g(\phi^n; \boldsymbol{\mu}). \tag{2.4}$$

Depending on the values of $\boldsymbol{\mu}$, solutions of this eighth order nonlinear partial differential equation lead to quasicrystals or periodic structures. For the latter, there are many fast algorithms. Specifically, the pseudospectral method achieves efficiency by evaluating the gradient terms in the Fourier space and the nonlinear terms in the physical space. On the other hand, the quasiperiodic structure cannot be solved directly by these classical methods suitable for the periodic structure. We adopt the projection method, the topic of the next section.

2.2. Phase-steady full order solutions based on the projection method. In the PM [21], a quasicrystal is first computed in a (higher-dimensional) reciprocal space as a periodic structure which is then projected back to the lower-dimensional space through the projection matrix. We provide a brief review of this approach.

One can represent the reciprocal vectors $\boldsymbol{k} \in \mathbb{R}^d$ of a d-dimensional quasicrystal as [4]

$$\boldsymbol{k} = h_1 \boldsymbol{p}_1^* + h_2 \boldsymbol{p}_2^* + \cdots + h_n \boldsymbol{p}_n^*, \quad h_i \in \mathbb{Z},$$

with $\boldsymbol{p}_i^* \in \mathbb{R}^d$ having $\mathbb{Z}$-rank of n[1] $(n > d)$. Different choices of the coefficient vector

$$\boldsymbol{h} \triangleq \{h_1, \cdots, h_n\}$$

(e.g., setting some of them to be zero and enforcing constraints on the others) lead to different quasicrystal patterns (see Figure 1). The PM finds proper n-dimensional vectors $\boldsymbol{b}_i^*, 1 \le i \le n$, being the primitive reciprocal vectors of the n-dimensional reciprocal space. The reciprocal vector of an n-dimensional periodic structure is then

$$\boldsymbol{H} = h_1 \boldsymbol{b}_1^* + h_2 \boldsymbol{b}_2^* + \cdots + h_n \boldsymbol{b}_n^*, \quad h_i \in \mathbb{Z}.$$

We denote by $\mathcal{S} \in \mathbb{R}^{d \times n}$ a projection matrix satisfying $\boldsymbol{p}_i^* = \mathcal{S} \boldsymbol{b}_i^*$.

This means that the d-dimensional quasicrystal is a periodic structure in the n-dimensional space. In this paper, we focus on the case that $n = 4$ and $d = 2$ and the quasicrystal is 12-fold (i.e., we take $q = 2\cos(\pi/12)$ in the free energy functional $\mathcal{F}(\phi(\boldsymbol{r}); c, q, \boldsymbol{\mu})$ (2.1). The primitive reciprocal vectors are $\boldsymbol{p}_1^* = (1, 0)$ and $\boldsymbol{p}_4^* = (0, 1)$ (see Figure 2). However, some reciprocal vectors of the 12-fold case cannot be represented as a linear combination of $\boldsymbol{p}_1^*$ and $\boldsymbol{p}_4^*$ with integral coefficients. We therefore adopt

$$\boldsymbol{p}_1^* = (1, 0), \quad \boldsymbol{p}_2^* = (\cos(\pi/6), \sin(\pi/6)), \quad \boldsymbol{p}_3^* = (\cos(\pi/3), \sin(\pi/3)), \quad \boldsymbol{p}_4^* = (0, 1)$$

of $\mathbb{Z}$-rank 4, and the projection matrix

$$\mathcal{S} = \begin{pmatrix} 1 & \cos(\pi/6) & \cos(\pi/3) & 0 \\ 0 & \sin(\pi/6) & \sin(\pi/3) & 1 \end{pmatrix}.$$

With this idea, the Fourier expansion for the d-dimendional quasiperiodic function is given by

$$\phi(\boldsymbol{r}) = \sum_{\boldsymbol{H}} \widehat{\phi}(\boldsymbol{H}) e^{i\left[(\mathcal{S}\cdot\boldsymbol{H})^T \cdot \boldsymbol{r}\right]}, \quad \boldsymbol{r} \in \mathbb{R}^d, \quad \boldsymbol{H} \in \mathbb{Z}^n. \tag{2.5}$$

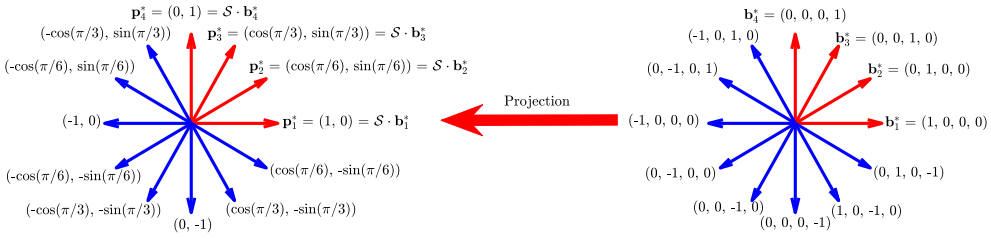

FIG. 2. *Reciprocal lattice vectors of* 12*-fold rotational symmetry in* 2*- and* 4*-dimensional space. The two sets of vectors are connected through the projection matrix* $\mathcal{S}$.

[1]The only $\{h_i \in \mathbb{Z}\}$ leading to $h_1 \boldsymbol{p}_1^* + h_2 \boldsymbol{p}_2^* + \cdots + h_n \boldsymbol{p}_n^* = 0$ is $h_i \equiv 0$.

Denoting by g_k^T the kth row of $\mathcal{S}\cdot\boldsymbol{H}$, we have that

$$\mathcal{S}\cdot\boldsymbol{H}=\left(\sum_{i=1}^{n}s_{1i}\sum_{j=1}^{n}h_jb_{ji}^*,\ldots,\sum_{i=1}^{n}s_{di}\sum_{j=1}^{n}h_jb_{ji}^*\right)^T\triangleq(g_1,\ldots,g_d)^T,\quad h_j\in\mathbb{Z},$$

with $b_{ji}^*, j=1,\ldots,n$ being the components of b_i^*. The LP free energy functional then becomes

(2.6)

$$\begin{aligned}\mathcal{F}(\phi(\boldsymbol{r});c,q,\boldsymbol{\mu})=&\frac{1}{2}\sum_{\boldsymbol{H}_1+\boldsymbol{H}_2=0}\left\{c\left(1-\sum_{k=1}^{d}g_k^2\right)^2\left(q^2-\sum_{k=1}^{d}g_k^2\right)^2-\varepsilon\right\}\widehat{\phi}(\boldsymbol{H}_1)\widehat{\phi}(\boldsymbol{H}_2)\\&-\frac{\alpha}{3}\sum_{\boldsymbol{H}_1+\boldsymbol{H}_2+\boldsymbol{H}_3=0}\widehat{\phi}(\boldsymbol{H}_1)\widehat{\phi}(\boldsymbol{H}_2)\widehat{\phi}(\boldsymbol{H}_3)\\&+\frac{1}{4}\sum_{\boldsymbol{H}_1+\boldsymbol{H}_2+\boldsymbol{H}_3+\boldsymbol{H}_4=0}\widehat{\phi}(\boldsymbol{H}_1)\widehat{\phi}(\boldsymbol{H}_2)\widehat{\phi}(\boldsymbol{H}_3)\widehat{\phi}(\boldsymbol{H}_4).\end{aligned}$$

Substituting (2.5) into (2.4) and using (2.6), one obtains

(2.7)

$$\begin{aligned}&\left(\frac{1}{\Delta t}+c\left(1-\sum_{k=1}^{d}g_k^2\right)^2\left(q^2-\sum_{k=1}^{d}g_k^2\right)^2\right)\widehat{\phi}_{t+\Delta t}(\boldsymbol{H})=\left(\frac{1}{\Delta t}+\varepsilon\right)\widehat{\phi}_t(\mathbf{H})\\&+\alpha\sum_{\boldsymbol{H}_1+\boldsymbol{H}_2=\boldsymbol{H}}\widehat{\phi}_t(\boldsymbol{H}_1)\widehat{\phi}_t(\boldsymbol{H}_2)-\sum_{\boldsymbol{H}_1+\boldsymbol{H}_2+\boldsymbol{H}_3=\boldsymbol{H}}\widehat{\phi}_t(\boldsymbol{H}_1)\widehat{\phi}_t(\boldsymbol{H}_2)\widehat{\phi}_t(\boldsymbol{H}_3),\end{aligned}$$

where Δt is the temporal step, and $\widehat{\phi}_{t+\Delta t}$ and $\widehat{\phi}_t$ represent the Fourier coefficients at time $t+\Delta t$ and t, respectively. A direct evaluation of the convolution terms of (2.7) are expensive. Instead, one can calculate these nonlinear terms in the physical space and then perform FFT to derive the corresponding Fourier coefficients. Therefore, the computational complexity of the PM is

$$O\left(N_t\cdot\mathcal{N}\log\mathcal{N}\right),$$

where N_t is the number of time iterations, and $\mathcal{N}=(N_{\boldsymbol{H}})^n$ with $N_{\boldsymbol{H}}$ being the degrees of freedom of the pseudospectral method in each dimension.

2.3. Phase diagram, phase transition, and multiple phase-steady solutions. The phase diagram is a quantitative and graphical representation of the stability and interconversion relationships of various metastable/stable phases of a material under different conditions, e.g., with different temperature ε and phenomenological parameter α. The phase field model can be used to not only simulate the phase transformation and microstructure changes during the processing and handling of materials, but also to predict the possible emergence of new materials or novel phases. However, it is quite time consuming to generate the phase diagram for a wide range of parameter values.

For each value of parameter $\boldsymbol{\mu}:=[\varepsilon,\alpha]$, due to the existence of the multiple stable solutions corresponding to the different prominent reciprocal vectors, one needs to solve (2.7) five times with five different initial values $\widehat{\phi}_0(\boldsymbol{\mathcal{H}}_{\mathrm{S}})$ corresponding to five candidate states $\boldsymbol{\mathcal{H}}_{\mathrm{S}}$ for $\mathrm{S}\in\{\mathrm{QC, C6, LQ, T6, Lam}\}$. The iteration initialized specifically based on the reciprocal vectors of each state allows for a rapid convergence of the gradient flow equation. Indeed, we denote by

$$\widehat{\phi}(\cdot;\boldsymbol{\mathcal{H}}_{\mathrm{S}},\boldsymbol{\mu})$$

TABLE 1
Prominent reciprocal vectors in four-dimensional space with nonzero initial Fourier coefficients.

$\lvert\mathcal{S}\cdot\mathbf{H}\rvert = 1$	(0 1 0 0)	**(0 0 1 0)**	(0 0 0 1)	**(-1 0 1 0)**	(0 -1 0 1)	**(-1 0 0 0)**
	(0 -1 0 0)	**(0 0 -1 0)**	(0 0 0 -1)	**(1 0 -1 0)**	(0 1 0 -1)	**(1 0 0 0)**
$\lvert\mathcal{S}\cdot\mathbf{H}\rvert = q$	(1 1 0 0)	(0 1 1 0)	(0 0 1 1)	(-1 0 1 1)	(-1 -1 1 1)	(-1 -1 0 1)
	(-1 -1 0 0)	(0 -1 -1 0)	(0 0 -1 -1)	(1 0 -1 -1)	(1 1 -1 -1)	(1 1 0 -1)

the steady-state solution for $\boldsymbol{\mu}$ with the initial value given by $\widehat{\phi}_0(\boldsymbol{\mathcal{H}}_{\mathrm{S}})$. As indicated in Figure 1(f), there are 24 prominent reciprocal vectors for S = QC. These two-dimensional reciprocal vectors can be transformed into four-dimensional space, and they are related by the projection matrix $\mathcal{S}$ (see Figure 2). For a more intuitive illustration, we display all the 24 prominent reciprocal vectors in four-dimensional space in Table 1, and the remaining sets $\boldsymbol{\mathcal{H}}_{\mathrm{S}}$'s for S $\in$ {C6, LQ, T6, Lam} are defined as follows. For S = C6, $\boldsymbol{\mathcal{H}}_{\mathrm{S}}$ contains the six reciprocal vectors displayed in bold. For S = LQ, it contains the 12 reciprocal vectors underlined. For S = T6, the six prominent reciprocal vectors are displayed with dash lines. The two reciprocal vectors for S = Lam are displayed with wavy lines. For a rapid convergence, the Fourier coefficients of these five sets of reciprocal vectors are initialized with nonzero values

$$\widehat{\phi}_0(\boldsymbol{\mathcal{H}}_{\mathrm{S}}) = u_0, \tag{2.8}$$

where u_0 is a given constant.

The set of *multiple phase-steady solutions* (PSS) corresponding to $\boldsymbol{\mu}$ is then

$$\widehat{\Phi}(\cdot;\boldsymbol{\mu}) \triangleq \bigcup_{\mathrm{S=QC}}^{\mathrm{Lam}} \left\{\widehat{\phi}(\cdot;\boldsymbol{\mathcal{H}}_{\mathrm{S}},\boldsymbol{\mu})\right\} \tag{2.9}$$

.Here, for simplicity, we define $\{\widehat{\phi}(\cdot;\boldsymbol{\mathcal{H}}_{\mathrm{S}},\boldsymbol{\mu})\}$ to be the empty set when $\widehat{\phi}$ goes through a phase transition with the given initial value $\widehat{\phi}_0(\boldsymbol{\mathcal{H}}_{\mathrm{S}})$. The rationale is that since each parameter leads to a stable state solution without phase transitions, the solutions that undergo phase transitions during the evolution process can be readily discarded.

The existence of multiple convergent solutions for the same $\boldsymbol{\mu}$ serves two purposes. On one hand, for the single-query setting, the state within $\widehat{\Phi}(\cdot;\boldsymbol{\mu})$ that leads to the smallest free energy functional is the stable state for the queried parameter. On the other hand, for the multiquery setting, the construction of the multiple components of our proposed MCMS-RBM takes advantage of the existence of the multiple solutions corresponding to the multiple states. The many-to-many pattern between components and states, a main novelty of the MCMS-RBM, enables the quick and simultaneous enriching of the reduced spaces with limited FOM queries. The detailed high-fidelity solver for

$$\boldsymbol{\mu} \mapsto \widehat{\Phi}(\cdot;\boldsymbol{\mu})$$

is shown in Algorithm 1.

This algorithm utilizes a phase transition indicator (PTI), which is given in Algorithm 2. It is inspired by the observation that, if the initial state is not in the stable state (out of the five possible states) corresponding to the given parameter, the evolution may or may not undergo a transition to other states. When the

Algorithm 1 FOM for the LP model, $\boldsymbol{\mu} \mapsto \widehat{\Phi}(\cdot;\boldsymbol{\mu})$.

Input: parameter $\boldsymbol{\mu}$, tolerance tol, temporal step Δt, and maximum iteration T
Set $\widehat{\Phi}(\cdot;\boldsymbol{\mu}) = \{\}$
For S $\in$ {QC, C6, LQ, T6, Lam}
  Initialize the Fourier coefficients $\widehat{\phi}_0$ corresponding to $\boldsymbol{\mathcal{H}}_{\mathrm{S}}$
  Initialize res $= 1$, $\mathrm{PTI}_S = 0$, and $t = 0$. Calculate $\phi_0 = \mathscr{F}^{-1}(\widehat{\phi}_0)$
  While res $\geq$ tol & $t \leq T$ & $\mathrm{PTI}_{\mathrm{S}} = 0$
    Obtain $\widehat{\phi}_{t+\Delta t}$ by (2.7) using $\widehat{\phi}_t$ and ϕ_t
    res $= \|\widehat{\phi}_{t+\Delta t} - \widehat{\phi}_t\|_2$
    $t = t + \Delta t$, $\phi_t = \mathscr{F}^{-1}(\widehat{\phi}_t)$
    $\mathrm{PTI}_{\mathrm{S}} = \mathrm{PTI}(\widehat{\phi}_0, \widehat{\phi}_t)$
  End While
  If $\mathrm{PTI}_{\mathrm{S}} = 0$, set $\widehat{\Phi}(\cdot;\boldsymbol{\mu}) = \widehat{\Phi}(\cdot;\boldsymbol{\mu}) \cup \{\widehat{\phi}_t\}$
End For
Output: High fidelity PSS set $\widehat{\Phi}(\cdot;\boldsymbol{\mu})$

Algorithm 2 Phase transition indicator, $\mathrm{PTI}\,(\widehat{\phi}_0, \widehat{\phi}_t)$.

Input: Reference state $\widehat{\phi}_0$, candidate $\widehat{\phi}_t$, and tolerance δ
Calculate the locations of the elements of $\widehat{\phi}_0$ with $|\widehat{\phi}_0| > \delta$
Calculate the locations of the elements of $\widehat{\phi}_t$ with $|\widehat{\phi}_t| > \delta$
If they coincide, then PTI $= 0$, otherwise, PTI $= 1$

transition happens, it deteriorates the low-rank nature of the corresponding branch of the solution manifold. We therefore discard the convergent solution whenever a phase transition occurs in the evolution process. The detection of such transitions is made possible by the realization that solutions sharing the same structure maintain consistent characteristics in their corresponding *spectral signature* (the set of spectral coefficients whose magnitudes are above a certain tolerance) throughout the entire evolution. The "emergence" or "disappearance" of a spectral mode therefore signifies a phase transition.

3. The MCMS-RBM. As detailed in section 2.2, the PM method can produce an accurate approximation of the quasicrystals by solving the LP model in a higher-dimensional reciprocal space while taking advantage of FFT to deal with the linear and nonlinear terms. However, determining a delicate phase diagram of the LP model is still expensive due to the wide range of parameters and the existence of multiple stable states. Although an adaptive method exists [18] that can generate the phase diagram without having to resolve the full parameter domain, it fails to produce the field variables $\widehat{\phi}$ and ϕ, which are needed, e.g., in controlling the self-assembly of quasicrystals and a variety of other desired structures in practical experimental realizations [1, 5, 24, 29].

The proposed MCMS-RBM strives to learn the parameter dependence of the PM solution, vastly accelerate the generation of the phase diagram, and furnish surrogate and equally accurate field variables anywhere in the parameter domain. The MCMS-RBM has two prominent features in comparison to the standard RBM. First, it has multiple components, with each providing reduction functionality for one branch of

the problem induced by one part of the parameter domain. Second, without resorting to the parameter domain configurations (e.g., phase diagrams) a priori, it enriches each component in a greedy fashion via a phase-transition guided exploration of the multiple states inherent to the problem. Specifically, it tests each stable state for every parameter value and retains all solutions that have not gone through any phase transitions. All these solutions, which are multiple for each parameter value, are adopted by the RBM components according to their convergent state.

We devote the rest of this section to the presentation of the two parts of the MCMS-RBM, namely, its online and offline procedures, the adaptive algorithm that we adopt from [18], and its enhancement by the MCMS-RBM.

A key strategy of the RBM is the offline-online decomposition. During the offline procedure, five low-dimensional RB spaces of dimensions N_{S}

$$W_{N_{\mathrm{S}}}^{\mathrm{S}} \text{ for each state } \mathrm{S} \in \{\mathrm{QC},\ \mathrm{C6},\ \mathrm{LQ},\ \mathrm{T6},\ \mathrm{Lam}\}$$

are generated by a greedy algorithm. These are called the five *components* of the MCMS-RBM. During the online procedure for any given parameter value $\boldsymbol{\mu}$, the unknown RB coefficients in each component are solved through a reduced order model with an initial value given in the corresponding *state*. Here, we first introduce the online procedure which will be repeatedly called during the offline construction phase to build $\{W_{N_{\mathrm{S}}}^{\mathrm{S}}\}$. To achieve online efficiency, we resort to the EIM [2, 12].

3.1. Empirical interpolation method. For an online efficient computation of the two nonlinear functions g and h, a greedy algorithm is employed. This algorithm identifies a function-specific ($\boldsymbol{\mu}$-independent) interpolation basis and corresponding interpolation points. The resulting EIM approximation interpolates each function using this function-specific basis at the chosen points:

$$g(\phi(\boldsymbol{x},t);\boldsymbol{\mu}) \approx g_{M_g}(\phi(\boldsymbol{x},t),t;\boldsymbol{\mu}) = \sum_{m=1}^{M_g} d_{M_g,m}(\boldsymbol{\mu},t)\, g(\boldsymbol{x};\boldsymbol{\mu}_g^m),$$

$$h(\phi(\boldsymbol{x},t);\boldsymbol{\mu}) \approx h_{M_h}(\phi(\boldsymbol{x},t),t;\boldsymbol{\mu}) = \sum_{m=1}^{M_h} \gamma_{M_h,m}(\boldsymbol{\mu},t)\, h(\boldsymbol{x};\boldsymbol{\mu}_h^m).$$

Here, $\{\boldsymbol{\mu}_g^m\}_{m=1}^{M_g}$ and $\{\boldsymbol{\mu}_h^m\}_{m=1}^{M_h}$ are two sets of parameter ensembles chosen by the greedy algorithm, while $g(\boldsymbol{x};\boldsymbol{\mu}_g^m)$ and $h(\boldsymbol{x};\boldsymbol{\mu}_h^m)$ are the corresponding functions that are orthonormal under point evaluations at the interpolation points.

Specifically to our developed MCMS-RBM, we construct one set of EIM expansions for each of the five states. Indeed, for each parameter initiated with each of the five states, the high-fidelity solution that has not gone through any phase transitions in the evolution will be adopted in the greedy procedure.

3.2. Online procedure. The MCMS-RBM approximates the high-fidelity solution with a surrogate solution

$$\widehat{\phi}(\boldsymbol{\mu},t) \approx \widehat{\phi}_{\mathrm{rb}}(\boldsymbol{\mu},t) = W_N c_N(\boldsymbol{\mu},t), \tag{3.1}$$

where W_N is one of the $W_{N_{\mathrm{S}}}^{\mathrm{S}}$'s. For simplicity, we omit the sub- and super-scripts S whenever there is no confusion. Moreover, c_N is the RB coefficient to be solved for that component whose notational dependence on S is also omitted. The inverse Fourier transform of this surrogate solution can be directly derived as

$$\phi(\boldsymbol{\mu},t) \approx i W_N c_N(\boldsymbol{\mu},t)$$

with iW_N representing the inverse Fourier transform of basis space W_N. Therefore, the repeated transformations in real and reciprocal spaces during the iteration will also be calculated in low-dimensional space and it is independent of the degrees of freedom of the FOM. For simplicity, we denote the unknown RB coefficients $c_N(\boldsymbol{\mu}, t)$ at iteration t by $c_t(\boldsymbol{\mu})$. Substituting these surrogate solutions and the EIM approximation into (2.7) and using the Galerkin projection method, one can derive the reduced order model

$$W_N^T\left(1+\Delta t\cdot c\left(1-\boldsymbol{k}^2\right)^2\left(q^2-\boldsymbol{k}^2\right)^2\right)W_N c_{t+1} = W_N^T(1+\Delta t\cdot\varepsilon)W_N c_t + \Delta t\cdot W_N^T\mathscr{F}(V_M^g d_t^M), \tag{3.2}$$

where $\boldsymbol{k}^2=\sum_{k=1}^d g_k^2$. Here, V_M^g is the basis space constructed by the EIM for $g(\phi(\boldsymbol{x},t);\boldsymbol{\mu})=\alpha\phi^2-\phi^3$, and d_t^M is the coefficient of the EIM at every iteration. We rewrite this equation as

$$A_1 c_{t+1} = A_2 c_t + \Delta t\cdot\varepsilon A_2 c_t + A_3 d_t^M, \tag{3.3}$$

where $A_1 = W_N^T(1+\Delta t\cdot c(1-\boldsymbol{k}^2)^2(q^2-\boldsymbol{k}^2)^2)W_N\in\mathbb{R}^{N\times N}$, $A_2=W_N^TW_N\in\mathbb{R}^{N\times N}$, and $A_3=\Delta t W_N^T\mathscr{F}(V_M^g)\in\mathbb{R}^{N\times M}$. We note that they can all be precomputed during the offline procedure via updates as each snapshot is identified. Further, they also depend on S but with notational dependence omitted.

The calculation of the free energy can also be accelerated since we have

$$E_{\mathrm{rb}} = \frac{c}{2}c_t^T E_1 c_t - \frac{\varepsilon}{2}c_t^T A_2 c_t + \left(\gamma_t^L\right)^T V_L^h\mathbf{1}, \tag{3.4}$$

where $E_1 = iW_N^T((1-\boldsymbol{k}^2)^2(q^2-\boldsymbol{k}^2)^2)^2 iW_N\in\mathbb{R}^{N\times N}$, V_L^h is the basis space of EIM for nonlinear terms of the free energy functional $h(\phi(\boldsymbol{x},t);\boldsymbol{\mu})=-\frac{\alpha}{3}\phi^3+\frac{1}{4}\phi^4$, γ_t^L is the coefficient of EIM at terminal time, and $\mathbf{1}$ is a column vector of 1's. The detailed online algorithm is provided in Algorithm 3.

The complexity of this procedure is

$$O(N_{t,\mathbf{RB}}\cdot(N^3+NM^2)),$$

where $N_{t,\boldsymbol{RB}}$ is the iteration times of the RBM, which is almost the same as the iteration times of solving the FOM. However, $O(M^2+N^3)$ is much smaller than

Algorithm 3 Online procedure of the MCMS-RBM.

1: **Input:** Precomputed reduced matrices A_1, A_2, A_3, and E_1 for a given S $\in$ {QC, C6, LQ, T6, Lam}, tolerance δ, parameter $\boldsymbol{\mu}$, temporal step Δt, and total time T
2: Initialize the Fourier coefficient $\widehat{\phi}_0$ for state S, and derive the initial RB coefficient c_0. Set res $=1$ and $t=0$
3: **While** res $\geq\delta$ and $t\leq T$
4: Calculate the EIM coefficient d_t^M for $\boldsymbol{\mu}$
5: Solve the RB coefficient $c_{t+\Delta t}$ by (3.3), and calculate res $=\|c_{t+\Delta t}-c_t\|_2$
6: $t=t+\Delta t$
7: **End While**
8: Calculate the EIM coefficient γ_t^L for $\boldsymbol{\mu}$
9: **Output:** Surrogate solution $\widehat{\phi}_{t,\mathrm{rb}}=W_N c_t$, $\phi_{t,\mathrm{rb}}=iW_N c_t$, and the free energy functional $E=\frac{c}{2}c_t^TE_1c_t-\frac{\varepsilon}{2}c_t^TA_2c_t+\left(\gamma_t^L\right)^TV_L^h\mathbf{1}$

$O(\mathcal{N}\log\mathcal{N})$ because $N^3 \ll \mathcal{N}$ and $NM^2 \ll \mathcal{N}$. Moreover, the surrogate solution obtained by the RBM is essentially an approximation of the truth solution at each moment, so asymptotically the phase transition between the surrogate solution and the high-fidelity solution occurs almost simultaneously.

3.3. Offline procedure. Now we present the greedy algorithm for constructing the RB spaces. For general nonlinear parametrized PDEs, designing a rigorous residual-based error estimator is far from trivial. By recalling that,

- the high order gradient term in the LP model ensures two-wavelength selection and is very important for pattern formation with two wavelength scales [25],
- the second term $\varepsilon\phi^2/2$, which corresponds to $\varepsilon\phi$ of (2.4), describes the growth of the instability, as appears in the Swift–Hohenberg model [34],
- the remaining two terms in $g(\phi;\boldsymbol{\mu})$ (see (2.4)) are higher order terms with its first term $\alpha\phi^2$ dominating and can be approximated by $2\alpha\phi$ when $\|\phi\|$ is small with ϕ representing the error between the FOM and RB solutions $\widehat{\phi} - \widehat{\phi}_{\mathrm{rb}}$.[2]

In our multiple-component multistate framework, the error estimator should reflect the two wavelength scales and capture the instability evolution. Therefore, the following error indicator is adopted:

$$\Delta_n(\boldsymbol{\mu}) := \frac{\|r_n(\boldsymbol{\mu})\|_2}{\beta(\boldsymbol{\mu})}. \tag{3.5}$$

This is inspired by the traditional residual-based error estimators [9, 13, 17, 31] yet reflects the particular nature of the problem we study in this paper. Specifically, we note the following.

- The denominator $\beta(\boldsymbol{\mu})$ is defined based on the first three terms of the nonlinear steady-state full order model corresponding to (2.4).

  $$\beta(\boldsymbol{\mu}) = \sigma_{\min}\left(\mathcal{A} - \varepsilon I - 2\alpha I\right)$$

  is the absolute value of the smallest eigenvalue of the matrix $\mathcal{A} - \varepsilon I - 2\alpha I$. $\mathcal{A}$ is a diagonal matrix and each of its diagonal elements corresponds to one of $c(1-\boldsymbol{k}^2)^2(q^2-\boldsymbol{k}^2)^2$, and I is the identity matrix. For this diagonal matrix, certain elements will be near zero for some values of the Fourier frequency, c, and parameter (ε,α). In these cases, the estimators may yield large numbers, and the corresponding parameters are then likely to be chosen by the greedy algorithm. This greedy selection is effective, and the resulting convergence rate and stability are better than those of other indicators such as the random selection and the nonscaled error estimator $\|r_n(\boldsymbol{\mu})\|_2$.
- Resorting to the gradient flow method, the residual r_n is defined as

  $$r_n(\boldsymbol{\mu}) = \mathcal{A}c_t - \varepsilon W_n c_t - \mathscr{F}(V_M^g)d_t^M.$$

  Note that the computational complexity of the residual's norm is made independent of $\mathcal{N}$ via an offline-online decomposition. Indeed, one has that

  $$\|r_n(\boldsymbol{\mu})\|_2^2 = c_t^T(B_1 - 2\varepsilon B_2 + \varepsilon^2 B_4)c_t + 2c_t^T(\varepsilon B_5 - B_3)d_t^M + (d_t^M)^T B_6 d_t^M, \tag{3.6}$$

[2]The contribution by the $\alpha\phi^2$ term to the residual is $\alpha(\widehat{\phi}+\widehat{\phi}_{\mathrm{rb}})(\widehat{\phi}-\widehat{\phi}_{\mathrm{rb}})$, which can be approximated by $2\alpha(\widehat{\phi}_{\mathrm{rb}})(\widehat{\phi}-\widehat{\phi}_{\mathrm{rb}})$ when the RB solution is more accurate (e.g., with a larger number of RB basis n). We further linearize and simplify this term in our calculation.

where $B_1 = \mathcal{A}^T\mathcal{A} \in \mathbb{R}^{n\times n}$, $B_2 = \mathcal{A}^T W_n \in \mathbb{R}^{n\times n}$, $B_3 = \mathcal{A}^T\mathscr{F}(V_M^g) \in \mathbb{R}^{n\times M}$, $B_4 = W_n^T W_n \in \mathbb{R}^{n\times n}$, $B_5 = W_n^T\mathscr{F}(V_M^g) \in \mathbb{R}^{n\times M}$, and $B_6 = (\mathscr{F}(V_M^g))^T\mathscr{F}(V_M^g) \in \mathbb{R}^{M\times M}$ can be precomputed and updated at each greedy loop. Afterward, the computation of the error indicator only depends on the numbers of the EIM and RB basis.

We are now ready to describe the greedy algorithm for constructing the five RB spaces $W_{N_\mathrm{S}}^\mathrm{S}$ with $\mathrm{S} \in \{\mathrm{QC}, \mathrm{C6}, \mathrm{LQ}, \mathrm{T6}, \mathrm{Lam}\}$. We first discretize the parameter domain $\mathcal{D}$ by a sufficiently fine training set Ξ_{train}. For any given S, the guiding principle is that the RB space $W_{N_\mathrm{S}}^\mathrm{S}$ should contain snapshots having the structure corresponding to the component S. Thus unlike the vanilla RBM, the first snapshot cannot be totally random. Indeed, this can be realized by performing Algorithm 1 for several parameters until the first $\boldsymbol{\mu}$ whose PSS (2.9) contains a branch corresponding to the current component S is identified. Next, we call the online solver for S via Algorithm 3 and calculate the error estimator for each parameter in the training set. The *temporary candidate* for the $(n+1)$th $(n = 1, 2, \ldots, N-1)$ parameter is selected as the maximizer of the error estimators

$$\boldsymbol{\mu}_{n+1}^{\mathrm{temp}} = \arg\max_{\boldsymbol{\mu}\in\Xi_{\mathrm{train}}} \Delta_n(\boldsymbol{\mu}).$$

We then call Algorithm 1, with initial value $\widehat{\phi}_0(\boldsymbol{\mathcal{H}}_\mathrm{S})$ to obtain the high-fidelity PSS $\widehat{\Phi}(\cdot;\boldsymbol{\mu}_{n+1}^{\mathrm{temp}})$. If this PSS contains a branch corresponding to S, that is, the phase transition does not happen, we enrich $W_{N_\mathrm{S}}^\mathrm{S}$ with this branch.[3] If $\widehat{\Phi}(\cdot;\boldsymbol{\mu}_{n+1}^{\mathrm{temp}})$ contains no S-specific component, we prune $\boldsymbol{\mu}_{n+1}^{\mathrm{temp}}$ and go to the next maximizer of the error indicators. This is repeated until we find a $\boldsymbol{\mu}_{n+1}^{\mathrm{temp}}$ whose PSS has a S-specific component. Finally, we set $\boldsymbol{\mu}_{n+1}$ to be this $\boldsymbol{\mu}_{n+1}^{\mathrm{temp}}$. The detailed greedy algorithm for the construction of the RB spaces $\{W_{N_\mathrm{S}}^\mathrm{S}\}$ is described in Algorithm 4.

Algorithm 4 Offline procedure of MCMS-RBM.

1: **Input:** training set Ξ_{train}, component S to be built
2: Select $\boldsymbol{\mu}_1$ from Ξ_{train} so that PSS $\widehat{\Phi}(\cdot;\boldsymbol{\mu}_1)$ has an S-state denoted by $\widehat{\phi}(\boldsymbol{\mu}_1)$. Initialize $S_1 = \boldsymbol{\mu}_1$, $W_1 = \{\widehat{\phi}(\boldsymbol{\mu}_1)/\|\widehat{\phi}(\boldsymbol{\mu}_1)\|_2\}$, $iW_1 = \mathscr{F}^{-1}(\widehat{\phi})/\|\mathscr{F}^{-1}(\widehat{\phi})\|_2$, and $n = 1$
3: **for** $n = 2, 3, \cdots, N-1$ **do**
4: Solve the RB coefficient in the S-component of the MCMS-RBM, $c_n(\boldsymbol{\mu})$, by (3.3) for each $\boldsymbol{\mu} \in \Xi_{\mathrm{train}}$, and calculate the error estimator through (3.5)
5: Choose $\boldsymbol{\mu}_{n+1}^{\mathrm{temp}} = \arg\max_{\boldsymbol{\mu}\in\Xi_{\mathrm{train}}} \Delta_n(\boldsymbol{\mu})$ and solve PSS $\widehat{\Phi}(\cdot;\boldsymbol{\mu}_{n+1}^{\mathrm{temp}})$ with the initial value $\widehat{\phi}_0(\boldsymbol{\mathcal{H}}_\mathrm{S})$ through Algorithm 1. If PSS is empty, one discards this parameter and chooses the next maximizer of the error indicators, until the one whose PSS has a component S is met. Set $\boldsymbol{\mu}_{n+1} = \boldsymbol{\mu}_{n+1}^{\mathrm{temp}}$, and $\widehat{\phi}_{n+1} = \mathrm{PSS}\,\widehat{\Phi}(\cdot;\boldsymbol{\mu}_{n+1})$
6: Update $S_{n+1} = \{S_n, \boldsymbol{\mu}_{n+1}\}$, $W_{n+1} = \mathrm{GS}(W_n, \widehat{\phi}_{n+1})$, $\phi_{n+1} = \mathscr{F}^{-1}(\widehat{\phi}_{n+1})$, $\eta_{n+1} = \phi_{n+1}/\|\phi_{n+1}\|_2$, $iW_{n+1} = \{iW_n, \eta_{n+1}\}$, and the reduced matrices $\{A_i\}_{i=1}^3, \{B_i\}_{i=1}^6$, and E_1
7: **end for**
8: **Output:** Reduced basis space W_n, the inverse RB space iW_n, and the reduced matrices $\{A_i\}_{i=1}^3, \{B_i\}_{i=1}^6$ and E_1

[3] In practice, we incorporate a Gram–Schmidt procedure for numerical robustness.

Algorithm 5 Adaptive phase diagram generation by the MCMS-RBM.

Input: tolerance δ_0, initial coarse grid Ξ_{diag}, size of current grid n_{diag}, number of iterations $n_{\text{adap}} = 0$, and distance index $d_{\text{adap}} = 2\delta_0$
While $d_{\text{adap}} > \delta_0$
Initialize boundary points $\Xi_{\text{diag,bp}} = \{\}$
Calculate free energy functional for all $\boldsymbol{\mu} \in \Xi_{\text{diag}}$ through Algorithm 3, and derive the current phase diagram
for $n = 1, 2, \ldots, n_{\text{diag}}$ **do**
    If the eight nearest neighbors of the nth point of Ξ_{diag}, $\Xi_{\text{diag}}(n)$ are in the same stable state of itself, then $I_{\text{bp}} = 0$; otherwise, $I_{\text{bp}} = 1$ and enrich $\Xi_{\text{diag,bp}} = \{\Xi_{\text{diag,bp}}, \Xi_{\text{diag}}(n)\}$
    If $I_{\text{bp}} = 1$, calculate all the middle points $\boldsymbol{\mu}_{\text{mid}}$ between $\Xi_{\text{diag}}(n)$ and its neighbors with different stable states. Enrich $\Xi_{\text{diag,bp}} = \{\Xi_{\text{diag,bp}}, \boldsymbol{\mu}_{\text{mid}}\}$
    Record the largest distance d_{adap} between points in $\Xi_{\text{diag,bp}}$ and their neighbors with different stable states
end for
Update $\Xi_{\text{diag}} = \Xi_{\text{diag,bp}}$, $n_{\text{adap}} = n_{\text{adap}} + 1$, $n_{\text{diag}} = |\Xi_{\text{diag}}|$
End While

3.4. Adaptive phase diagram generation by the MCMS-RBM. One advantage of building an efficient surrogate solver such as the developed MCMS-RBM is that it makes feasible the generation of phase diagrams via an exhaustive sampling of the parameter domain. We propose to further leverage the efficiency of the MCMS-RBM by adopting the adaptive strategy [18] when querying the parameter domain. The idea is to first sample a coarse cartesian grid to determine the phase of each point, and then for each point one checks the eight nearest neighbors. If all of them are identified as the same phase, one labels this point as an internal point. Otherwise, one regards the current point as a boundary point. The largest distance between this boundary point and its neighboring points with different stable states is recorded. For the next refinement, one appends the middle point between this boundary point and its neighboring points with different stable states, along with all the current boundary points, to form the new set for the next loop. Then one proceeds to identify all these points as internal and boundary points, enriching a new set for a new adaptive loop. We remark that, as the adaptive algorithm proceeds, the grid will become more unstructured, making the "eight nearest neighbors" not as easily identifiable as the initial structured grid. In this case, we simply sort the neighbors by its Euclidean distances to the base point. This adaptive refinement algorithm is provided in Algorithm 5. It ends when the boundaries between different states are considered resolved, which is defined to be that the distance between two points that are along the boundary but have different states is small enough.

4. Numerical results. In this section, we test the proposed MCMS-RBM on the two-dimensional quasiperiodic LP model parameterized by the reduced temperature ε and the phenomenological parameter α delineating the level of asymmetry. Furthermore, we highlight its efficiency and accuracy by adopting the adaptive phase diagram generation algorithm to produce a phase diagram that is as accurate as the state of the art.

4.1. Setup and notation. The parameter domain is set to be $\mathcal{D} = [-0.0125, 0.0515] \times [0, 1]$. The training and testing sets for constructing the EIM and RB spaces are $\mathcal{D}$'s two disjoint uniform cartesian discretizations,

$$\Xi_{\text{train}} = (-0.0125 : 0.002 : 0.0515) \times (0 : 0.05 : 1),$$
$$\Xi_{\text{test}} = (-0.01 : 0.015 : 0.05) \times (0.025 : 0.1 : 0.925).$$

For the high-fidelity solver of the LP model, we set the degree of freedom of the Fourier spectral method in each direction as $N_{\mathbf{H}} = 32$. We denote the worst-case relative errors of the nonlinear terms with m- dimensional space V_M^g by $\phi_{\text{err}}^g(m)$, and solutions and free energy functionals with n- dimensional space W_n by $\phi_{\text{err}}(n)$ and $E_{\text{err}}(n)$, respectively.

$$\phi_{\text{err}}^g(m) = \max_{\boldsymbol{\mu} \in \Xi_{\text{train}}} \left\{ \frac{\|g(\boldsymbol{\mu}) - g_{M_g}(\boldsymbol{\mu})\|_2}{\|g(\boldsymbol{\mu})\|_2} \right\},$$
$$\phi_{\text{err}}(n) = \max_{\boldsymbol{\mu} \in \Xi_{\text{test}}} \left\{ \frac{\|\widehat{\phi}(\boldsymbol{\mu}) - \widehat{\phi}_{n,rb}(\boldsymbol{\mu})\|_2}{\|\widehat{\phi}(\boldsymbol{\mu})\|_2} \right\},$$
$$E_{\text{err}}(n) = \max_{\boldsymbol{\mu} \in \Xi_{\text{test}}} \left\{ \frac{\|\mathcal{F}(\widehat{\phi}(\boldsymbol{\mu})) - \mathcal{F}(\widehat{\phi}_{n,rb}(\boldsymbol{\mu}))\|}{|\mathcal{F}(\widehat{\phi}(\boldsymbol{\mu}))|} \right\}.$$

Finally, we denote by $\Delta_{RB}(n)$ the worst-case error indicators when the RB spaces are of n-dimensional,

$$\Delta_{RB}(n) = \max_{\boldsymbol{\mu} \in \Xi_{\text{train}}} \Delta_n(\boldsymbol{\mu}).$$

4.2. MCMS-RBM results. We are now ready to present the numerical results of the MCMS-RBM applied to the parameterized two-dimensional quasiperiodic LP model.

EIM results. The relative error curves of the nonlinear terms in the LP model and the distribution of the first $M(= 30)$ selected parameters for each of the five MCMS-RBM components are showed in Figures 3 and 4. As expected, the error curves exhibit exponential convergence as the number of the EIM basis increases. It is worth noting that all five states can effectively limit the error to within 10^{-4} using just up to 30 basis functions. This allows for significant speedup for the reduced model. As to the distribution of the chosen parameter values, the selected parameters predominantly lie within the corresponding state of their phase diagrams for relatively simple structures like Lam (Figure 4(e)). However, for other complex structures such as QC and LQ (Figure 4(a), (c)), some parameters are chosen from other states and with a more uniform distribution with clusters toward the boundary. In Figure 4(f), the histogram is displayed to show the number of parameters distributed in different states. These results underscore *the many-to-many feature between components and states* of the developed MCMS-RBM.

RBM results. In Figure 5(a), (b), we present the error indicators and relative errors during the offline training stage. Initially, when the number of RB basis is insufficient, the solution manifold for each state is far from being resolved. The noncoercive nature of the problem causes the estimator to oscillate. After this initial phase, the decrease and saturation stages of the error indicator in Figure 5(a) and those of the actual error in Figure 5(b) are well-aligned. This includes the order of each state going into its stagnation stage. Moreover, when we omit the oscillation stage (of the first 5 or 6 bases) in Figure 5(a), the starts of saturation in both Figure 5(a) and (b)

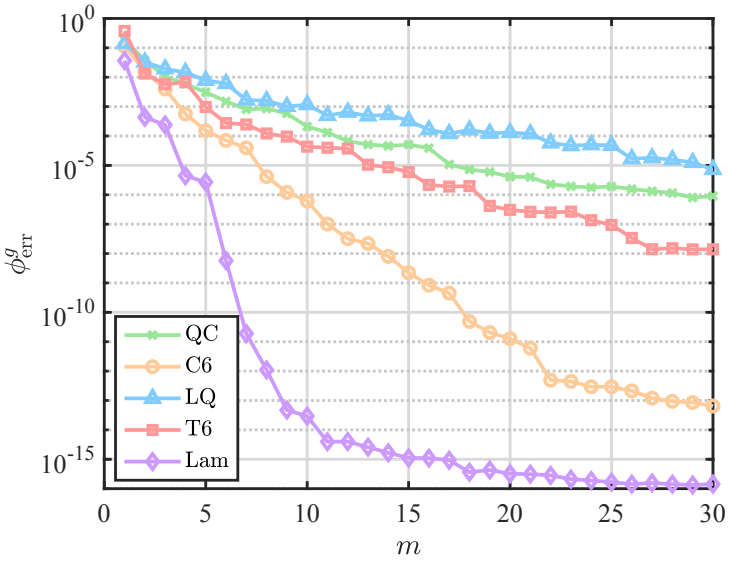

FIG. 3. *Relative EIM errors.*

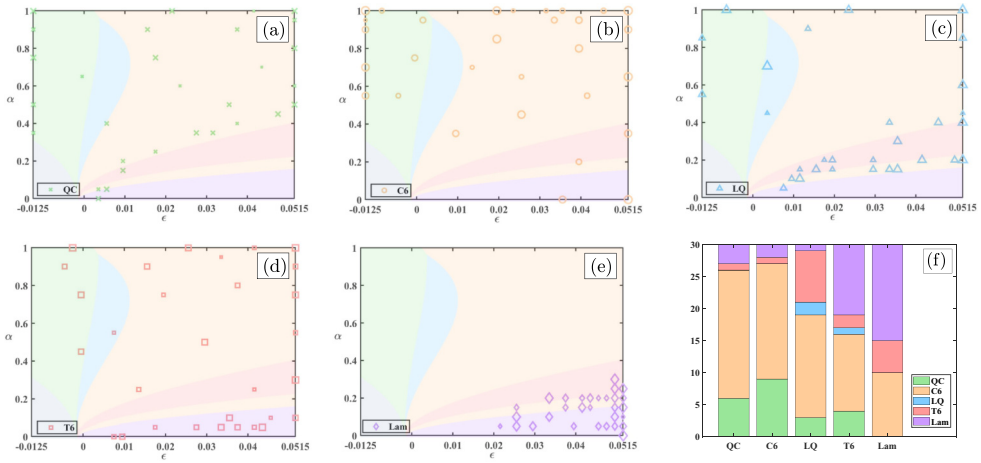

FIG. 4. *Distributions of the parameters selected by EIM corresponding to phases QC, C6, LQ, T6, and Lam* (a)–(e)*, and the histogram of each set of basis* (f).

are nearly the same. The consistency in convergence features in both figures further indicates the effectiveness of the proposed estimator. The efficiency of the error indicator and the accuracy of the MCMS-RBM are also underscored by the observed stable exponential convergence that the relative error curves exhibit right from the beginning. Furthermore, the relative errors of the solution with only 15 bases can reach 10^{-3}. The testing errors, in both the solution and the functional, are shown in Figure 5(c), (d). They, too, decrease exponentially. The distribution of the selected parameters of the RBM is shown in Figure 6. One notes that, just like the distributions of parameters in the EIM process shown in Figure 4 and RB studies of other equations, the chosen parameters are unstructured. The *many-to-many feature between components and states* also resembles that of the EIM process.

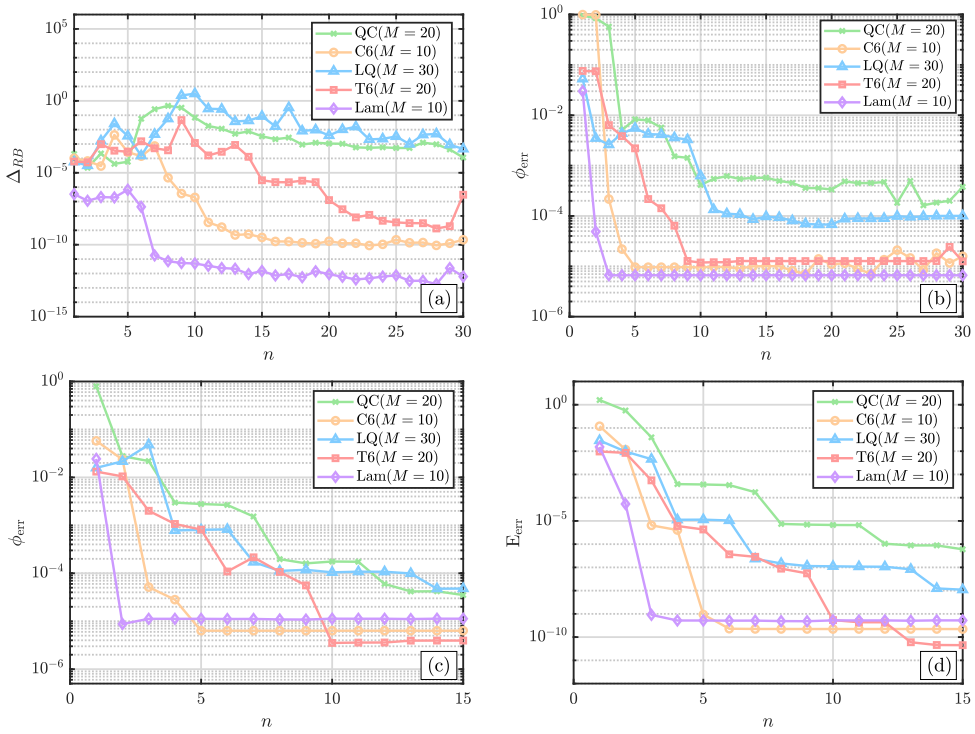

FIG. 5. *Training* (a)–(b) *and testing* (c)–(d) *results of MCMS-RBM. Top: Error indicators* (a) *and relative error curves during training* (b). *Bottom: Relative testing error curves of the solutions* (c) *and free energy functional* (d).

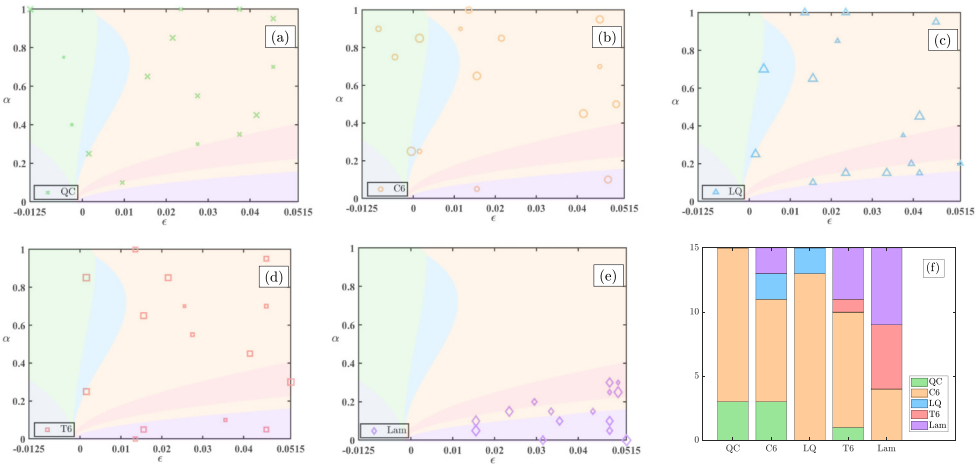

FIG. 6. *Distributions of the parameters selected by MCMS-RBM corresponding to phases QC, C6, LQ, T6, and Lam* (a)-(e), *and the histogram of each set of basis* (f).

Finally, we select five different parameters with one from each phase and apply our MCMS-RBM online solver to the corresponding LP model. We present in Table 2 the EIM/RB dimensions, the wall clock times for the full problem and the reduced problem, the offline time, the "break-even" number, and the MCMS-RBM errors in the

TABLE 2

Online computation time (in seconds), offline time (in seconds), break-even numbers, and relative error for the LP model at different parameters with $\Delta t = 0.1$ *and* $N_{\boldsymbol{H}} = 32$. *The degrees of freedom of the CAM and PM are* 1024^2 *and* 32^4, *respectively, with the CAM producing less-accurate solutions than the PM (see* [21]*).*

$\boldsymbol{\mu}$	$(5 \times 10^{-6}, \sqrt{2}/2)$	$(0.05, 1)$	$(0.005, 0.6)$	$(0.05, 0.3)$	$(0.05, 0.1)$
Phase	QC	C6	LQ	T6	Lam
(M, N)	(20,15)	(10,5)	(30,15)	(20,10)	(10,5)
PM time	4.51e+01	1.04e+01	7.47e+01	4.80e+01	4.16e+01
CAM time	3.28e+01	7.78e+00	5.20e+01	3.31e+01	2.85e+01
RBM time	3.24e-02	1.14e-02	5.08e-02	2.18e-02	1.29e-02
Offline time	6.88e+04	3.49e+04	6.77e+04	3.73e+04	8.38e+04
break-even num. PM	513	593	591	545	214
break-even num. CAM	694	657	782	774	288
ϕ_{err}	4.06e-06	4.23e-08	1.63e-05	5.68e-05	5.23e-09
E_{err}	4.32e-11	9.19e-12	2.72e-09	5.87e-12	1.06e-14

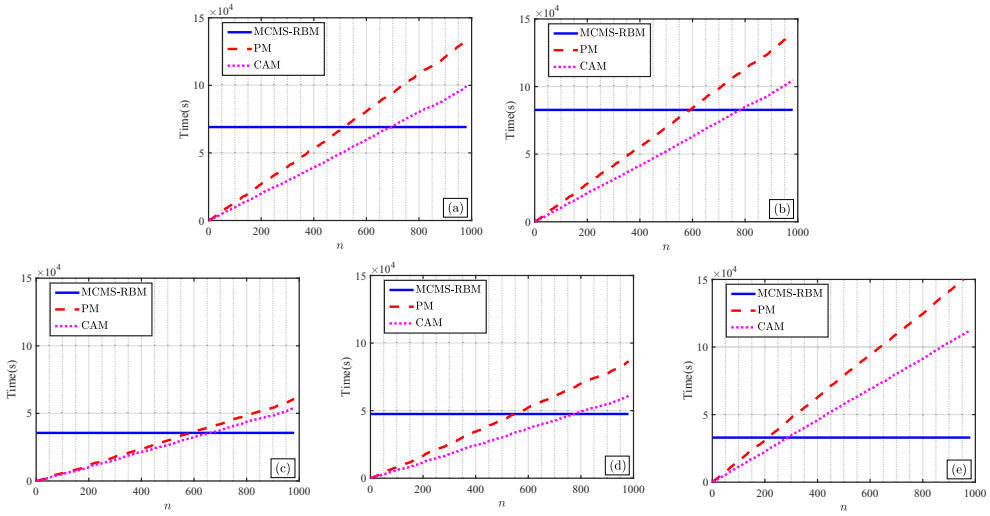

FIG. 7. *Cumulative runtime of the MCMS-RBM, the PM, and the CAM of components* QC, LQ, C6, T6, *and* Lam (a)–(e).

order parameter ϕ and the energy functional $\mathcal{F}$. For a more intuitive observation, we display in Figure 7 the cumulative computation time for the MCMS-RBM, the PM [18], and the CAM [39]. The initial nonzero start of the MCMS-RBM corresponds to the offline time and the intersection point is the break-even number, which measures, for each state, the critical number of solves after which the MCMS-RBM will begin to recoup the offline time. For example, we observe that, for the QC state when $n > 287$ and $n > 630$, the MCMS-RBM starts to save time in comparison to the repeated runs of the underlying PM and CAM solvers, respectively. We note that this break-even number can be further decreased, with the limit being of the order of $O(N + M)$, with a more efficient implementation of the offline algorithm. For example, for our EIM implementation, we generate full order solutions for the entire training set Ξ_{train}. This is not necessary. Producing the most optimal implementation is not the focus of this paper, but rather the methodology design of the MCMS-RBM. However, the

MCMS-RBM consistently achieves an acceleration of three orders of magnitude online while both relative errors are at levels of 10^{-5} and 10^{-9} with respect to the accuracy of the PM. Moreover, when the goal is the phase diagram generation (see section 4.3), even our suboptimal implementation would save computation time by two orders of magnitude.

4.3. Phase diagram generation. We now apply the adaptive phase generation algorithm of section 3.4 to our parametric LP model with the EIM and RB dimensions given as in Table 2. The initial phase diagram on a uniform coarse grid is generated by repeatedly invoking the online solver of the MCMS-RBM (see Figure 8(a)). Then the adaptive refinement is performed along the automatically detected boundaries of adjacent phases (see Algorithm 5). The bottom row of Figure 8 contains the results of three consecutive refinements, with the third one capturing the delicate boundaries of the phase diagram quite well. The numbers of repeated solves corresponding to Figure 8(a) and (c)–(e) are $n = 693, 981, 1829$, and 3333. We emphasize that all these phase diagrams are generated by only using the reduced solutions which are formed by just 50 (which is equal to the sum of RB dimensions for all components) FOM solutions. It is clear, by comparing with Table 2, that the MCMS-RBM starts saving time from the second refinement since we are well above the corresponding break-even number. In comparison, we query MCMS-RBM on a highly refined discretization of the parameter domain, a 601×501 uniform grid. See Figure 8(b) for the resulting phase diagram. It is clear that the third iteration of the adaptive algorithm agrees with this fine phase diagram, which is in turn consistent with that in [39].

As evidence of the efficiency of the adaptive algorithm, we list the wall clock time (in seconds) of each iteration in Table 3. It is clear that the generation of the coarse diagram only takes 120.31 seconds, and this value will increase when one performs

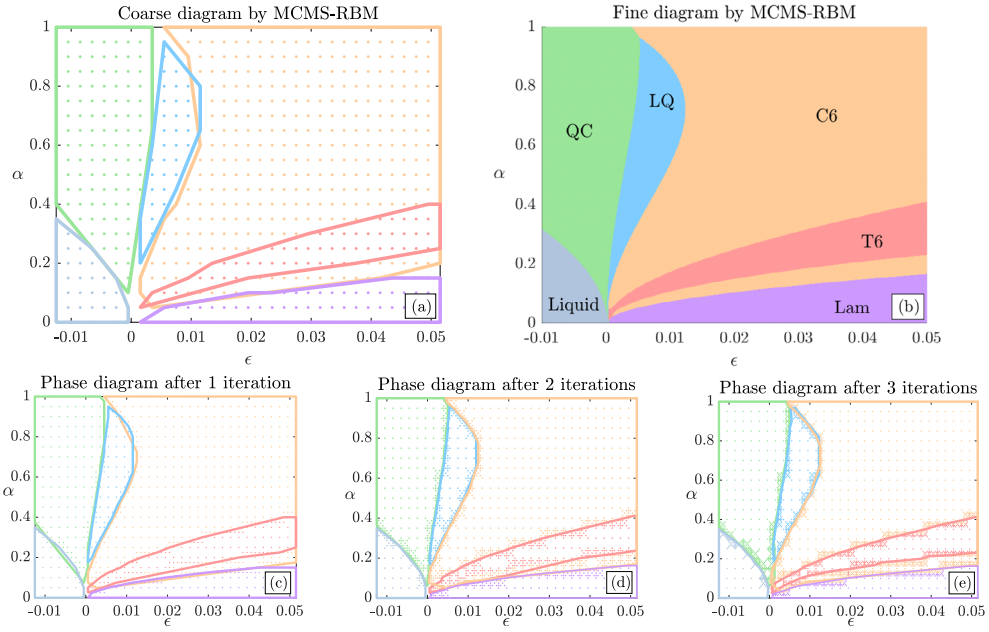

FIG. 8. *The iterative phase diagrams* (a), (c)–(e) *generated by the adaptive MCMS-enhanced algorithm. Shown on the top right* (b) *is a phase diagram with high resolution.*

TABLE 3
Online computation time (in seconds) for the adaptive boundary refinement algorithm. See Table 2 for the offline time.

Phase	QC	C6	LQ	T6	Lam	Total
Coarse	31.79	9.90	40.88	18.24	12.06	112.87
1st iteration	9.59	4.02	9.30	6.28	3.02	32.21
2nd iteration	25.30	9.92	15.41	10.83	2.81	64.27
3rd iteration	26.62	15.86	25.45	17.45	3.11	88.49

one more iteration, as shown in the 7th column of the table. The total time of the generation of Figure 8(e) is 297.84, which is derived by summarizing all the values of the 7th column. Indeed, the 601×501 fine phase diagram takes about 16 hours in a serial environment by MCMS-RBM. A simple scaling with the acceleration rate of Table 2 indicates that this phase diagram would have taken over 40 months to generate if we were to call the FOM solver repeatedly without the adaptive refinement technique. In a word, the computational cost of the phase diagram is significantly reduced by the MCMS-RBM and it can be further reduced by the adaptive refine boundary algorithm.

5. Conclusion. This paper proposes a multicomponent multistate reduced basis method (MCMS-RBM) for the parametrized quasiperiodic LP model with two length scales. Featuring multiple components with each providing a reduced order model for one branch of the problem induced by one part of the parameter domain, the MCMS-RBM serves as a generic framework for reduced order modeling of parametric problems whose solution has multiple states across the parameter domain.

Via a greedy algorithm that identifies the representative parameter values and a phase transition indicator, the method searches for the (potentially multiple) phase-steady solutions for each parameter value, which are then used to enrich the corresponding components of the MCMS-RBM. Numerical experiments corroborate that the method can provide surrogate and equally accurate field variables, with speedup of three orders of magnitude, anywhere in the parameter domain. It can also accelerate the generation of a delicate phase diagram to a matter of minutes.

REFERENCES

[1] K. Barkan, H. Diamant, and R. Lifshitz, *Stability of quasicrystals composed of soft isotropic particles*, Phys. Rev. B, 83 (2011), 172201.
[2] M. Barrault, Y. Maday, N. C. Nguyen, and A. T. Patera, *An empirical interpolation method: Application to efficient reduced-basis discretization of partial differential equations*, C. R. Math. Acad. Sci. Paris, 339 (2004), pp. 667–672.
[3] S. Brazovskii and S. Dmitriev, *Phase transitions in cholesteric liquid crystals*, Zh. Eksp. Teor. Fiz., 69 (1975), pp. 979–989.
[4] P. M. Chaikin, T. C. Lubensky, and T. A. Witten, *Principles of Condensed Matter Physics*, Cambridge University Press, Cambridge, 1995.
[5] L.-Q. Chen, *Phase-field models for microstructure evolution*, Ann. Rev. Mater. Res., 32 (2002), pp. 113–140.
[6] Y. Chen, S. Gottlieb, L. Ji, and Y. Maday, *An EIM-degradation free reduced basis method via over collocation and residual hyper reduction-based error estimation*, J. Comput. Phys., 444 (2021), 110545, https://doi.org/10.1016/j.jcp.2021.110545.
[7] Y. Chen, L. Ji, A. Narayan, and Z. Xu, *L1-based reduced over collocation and hyper reduction for steady state and time-dependent nonlinear equations*, J. Sci. Comput., 87 (2021), 10.
[8] Y. Chen, L. Ji, and Z. Wang, *A hyper-reduced MAC scheme for the parametric Stokes and Navier-Stokes equations*, J. Comput. Phys., 466 (2022), 111412.

[9] L. Dede, *Reduced basis method and a posteriori error estimation for parametrized linear-quadratic optimal control problems*, SIAM J. Sci. Comput., 32 (2010), pp. 997–1019.
[10] S. Deparis and G. Rozza, *Reduced basis method for multi-parameter-dependent steady Navier–Stokes equations: Applications to natural convection in a cavity*, J. Comput. Phys., 228 (2009), pp. 4359–4378.
[11] Z. Gao, Z. Xu, Z. Yang, and F. Ye, *Pythagoras superposition principle for localized eigenstates of two-dimensional Moiré lattices*, Phys. Rev. A (3), 108 (2023), 013513.
[12] M. A. Grepl, Y. Maday, N. C. Nguyen, and A. T. Patera, *Efficient reduced-basis treatment of nonaffine and nonlinear partial differential equations*, ESAIM Math. Model. Numer. Anal., 41 (2007), pp. 575–605.
[13] M. A. Grepl and A. T. Patera, *A posteriori error bounds for reduced-basis approximations of parametrized parabolic partial differential equations*, ESAIM Math. Model. Numer. Anal., 39 (2005), pp. 157–181.
[14] B. Haasdonk and M. Ohlberger, *Reduced basis method for finite volume approximations of parametrized linear evolution equations*, ESAIM Math. Model. Numer. Anal., 42 (2008), pp. 277–302.
[15] K. Hayashida, T. Dotera, A. Takano, and Y. Matsushita, *Polymeric quasicrystal: Mesoscopic quasicrystalline tiling in ABC star polymers*, Phys. Rev. Lett., 98 (2007), 195502.
[16] J. S. Hesthaven, G. Rozza, and B. Stamm, *Certified Reduced Basis Methods for Parametrized Partial Differential Equations*, Springer Briefs Math. 590, Springer, Berlin, 2016.
[17] D. B. P. Huynh, D. J. Knezevic, and A. T. Patera, *A static condensation reduced basis element method: Approximation and a posteriori error estimation*, ESAIM Math. Model. Numer. Anal., 47 (2013), pp. 213–251.
[18] K. Jiang and W. Si, *Automatically Generating Phase Diagram (AGPD),* v1, National Copyright Administration of the People's Republic of China 2022SR0139033, 2022, https://github.com/KaiJiangMath/AGPD.
[19] K. Jiang, W. Si, C. Chen, and C. Bao, *Efficient numerical methods for computing the stationary states of phase field crystal models*, SIAM J. Sci. Comput., 42 (2020), pp. B1350–B1377.
[20] K. Jiang, J. Tong, P. Zhang, and A.-C. Shi, *Stability of two-dimensional soft quasicrystals in systems with two length scales*, Phys. Rev. E (3), 92 (2015), 042159.
[21] K. Jiang and P. Zhang, *Numerical methods for quasicrystals*, J. Comput. Phys., 256 (2014), pp. 428–440.
[22] K. Jiang, P. Zhang, and A.-C. Shi, *Stability of icosahedral quasicrystals in a simple model with two-length scales*, J. Phys., 29 (2017), 124003.
[23] D. Levine and P. J. Steinhardt, *Quasicrystals: A new class of ordered structures*, Phys. Rev. Lett., 53 (1984), 2477.
[24] R. Lifshitz and H. Diamant, *Soft quasicrystals—Why are they stable?*, Philos. Mag., 87 (2007), pp. 3021–3030.
[25] R. Lifshitz and D. M. Petrich, *Theoretical model for Faraday waves with multiple-frequency forcing*, Phys. Rev. Lett., 79 (1997), 1261.
[26] A. K. Noor and J. M. Peters, *Reduced basis technique for nonlinear analysis of structures*, AIAA J., 18 (1980), pp. 455–462.
[27] V. Percec, M. R. Imam, M. Peterca, D. A. Wilson, R. Graf, H. W. Spiess, V. S. Balagurusamy, and P. A. Heiney, *Self-assembly of dendronized triphenylenes into helical pyramidal columns and chiral spheres*, J. Amer. Chem. Soc., 131 (2009), pp. 7662–7677.
[28] V. Percec, M. R. Imam, M. Peterca, D. A. Wilson, and P. A. Heiney, *Self-assembly of dendritic crowns into chiral supramolecular spheres*, J. Amer. Chem. Soc., 131 (2009), pp. 1294–1304.
[29] N. Provatas and K. Elder, *Phase-Field Methods in Materials Science and Engineering*, John Wiley & Sons, New York, 2011.
[30] A. Quarteroni, A. Manzoni, and F. Negri, *Reduced Basis Methods for Partial Differential Equations: An introduction*, Springer Ser. Comput. Math. 92, Springer, New York, 2015.
[31] G. Rozza, D. B. P. Huynh, and A. T. Patera, *Reduced basis approximation and a posteriori error estimation for affinely parametrized elliptic coercive partial differential equations: Application to transport and continuum mechanics*, Arch. Comput. Methods Eng., 15 (2008), 229.
[32] D. Shechtman, I. Blech, D. Gratias, and J. W. Cahn, *Metallic phase with long-range orientational order and no translational symmetry*, Phys. Rev. Lett., 53 (1984), pp. 1951–1953.
[33] W. Steurer, *Twenty years of structure research on quasicrystals. Part* I. *Pentagonal, octagonal, decagonal and dodecagonal quasicrystals*, Z. Kristallographie-Crystalline Mater., 219 (2004), pp. 391–446.

[34] J. Swift and P. C. Hohenberg, *Hydrodynamic fluctuations at the convective instability*, Phys. Rev. A, 15 (1977), 319.
[35] D. V. Talapin, E. V. Shevchenko, M. I. Bodnarchuk, X. Ye, J. Chen, and C. B. Murray, *Quasicrystalline order in self-assembled binary nanoparticle superlattices*, Nature, 461 (2009), pp. 964–967.
[36] A. P. Tsai, *Icosahedral clusters, icosaheral order and stability of quasicrystals—A view of metallurgy*, Sci. Technol. Adv. Mater., 9 (2008), 013008.
[37] K. Veroy, C. Prud'Homme, and A. T. Patera, *Reduced-basis approximation of the viscous Burgers equation: Rigorous a posteriori error bounds*, C. R. Math. Acad. Sci. Paris, 337 (2003), pp. 619–624.
[38] S. Walter and S. Deloudi, *Crystallography of Quasicrystals: Concepts, Methods and Structures*, Springer Ser. Mater. Sci. 126, Springer, New York, 2009.
[39] J. Yin, K. Jiang, A. Shi, P. Zhang, and L. Zhang, *Transition pathways connecting crystals and quasicrystals*, Proc. Natl. Acad. Sci. USA, 118 (2021), e2106230118.
[40] X. Zeng, G. Ungar, Y. Liu, V. Percec, A. E. Dulcey, and J. K. Hobbs, *Supramolecular dendritic liquid quasicrystals*, Nature, 428 (2004), pp. 157–160.
[41] J. Zhang and F. S. Bates, *Dodecagonal quasicrystalline morphology in a poly (styrene-b-isoprene-b-styrene-b-ethylene oxide) tetrablock terpolymer*, J. Amer. Chem. Soc., 134 (2012), pp. 7636–7639.
[42] P. Zhang and X. Zhang, *An efficient numerical method of Landau–Brazovskii model*, J. Comput. Phys., 227 (2008), pp. 5859–5870.
[43] Y. Zhou, H. Chen, and A. Zhou, *Plane wave methods for quantum eigenvalue problems of incommensurate systems*, J. Comput. Phys., 384 (2019), pp. 99–113.